

# Vision-Based Guidance for Tracking Dynamic Objects

Pritam Karmokar<sup>1\*</sup>, Kashish Dhal<sup>2\*</sup>, William J. Beksi<sup>1</sup>, and Animesh Chakravarthy<sup>2</sup>

**Abstract**—In this paper, we present a novel vision-based framework for tracking dynamic objects using guidance laws based on a rendezvous cone approach. These guidance laws enable an unmanned aircraft system equipped with a monocular camera to continuously follow a moving object within the sensor's field of view. We identify and classify feature point estimators for managing the occurrence of occlusions during the tracking process in an exclusive manner. Furthermore, we develop an open-source simulation environment and perform a series of simulations to show the efficacy of our methods.

## I. INTRODUCTION

In recent years there has been an increase in the number of applications using unmanned aircraft systems (UASs). At the same time, researchers have progressively inclined towards using vision as a primary source of perception [1]. This is mainly due to cameras becoming cheaper in cost, smaller in size, lighter in weight, and higher in image resolution. Likewise, as computing resources evolve to be more economical and powerful, there has been growing interest in research and development for UASs. On account of their agility, mobility, and form factor, various diverse problems have found UASs with on-board vision-based sensors to be an ideal solution [2]. Not only can UASs reach places that are intractable for humans to access, but they are also excellent platforms for monotonous and dangerous jobs. This includes traffic monitoring [3, 4], search and rescue [5, 6], reconnaissance for military operations [7, 8], and much more.

In this work, we construct a system that permits a UAS to pursue a dynamic ground vehicle using only visual information. To do this we employ the concept of a rendezvous cone. Concretely, we analytically show how a rendezvous cone can be used to develop guidance laws for a UAS to track a moving vehicle. These guidance laws are supported by a comprehensive set of computer vision algorithms that perform feature detection, track and make adjustments to the centroid of the vehicle, and filter for robustness and recovery through partial and full occlusions. In summary, our key contributions are the following.

- We introduce a set of systematic guidance laws which allow a UAS to visually track a moving object.

\*Indicates equal contribution

<sup>1</sup> P. Karmokar and W.J. Beksi are with the Department of Computer Science and Engineering, University of Texas at Arlington, Arlington, TX, USA. Emails: pritam.karmokar@mavs.uta.edu, william.beksi@uta.edu

<sup>2</sup> K. Dhal and A. Chakravarthy are with the Department of Mechanical and Aerospace Engineering, University of Texas at Arlington, Arlington, TX, USA. Emails: kashish.dhal@mavs.uta.edu, animesh.chakravarthy@uta.edu

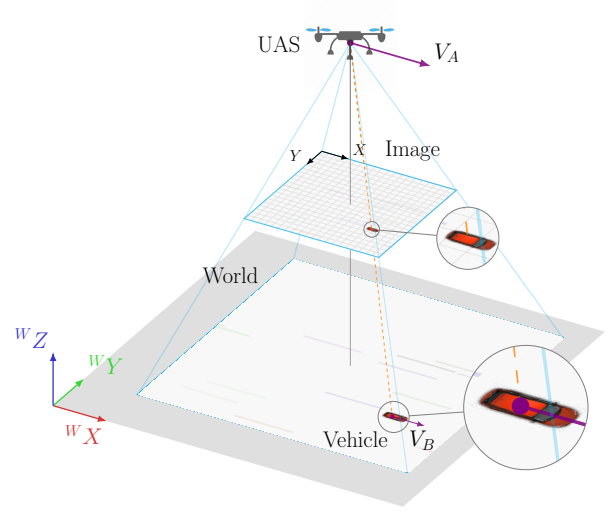


Fig. 1. Our proposed framework allows an unmanned aircraft system to visually track a ground vehicle under the existence of partial and total occlusions using unique guidance laws based on a rendezvous cone approach.

- We provide an identification and taxonomy of occlusion handling for feature point estimators under various occlusion cases.
- We implement an extensive open-source simulator [9] that supplies visual measurements while performing object tracking.

Moreover, our proposed system can be applied to applications such as tracking, monitoring, and surveillance via UASs.

The remainder of this paper is organized as follows. We discuss related work in Section II. Section III provides a concise statement of the problem to be solved. Our vision-based guidance scheme is presented in Section IV. In Section V, we report our simulation results. We conclude in Section VI and mention future work.

## II. RELATED WORK

### A. Cones in Relative Velocity Space

There has been related work on the development of guidance laws using cones constructed in the relative velocity space. The concept of collision cones was proposed in [10] to represent a collection of velocity vectors of an object which leads to a collision with another moving object. Guidance laws to avoid collision were then designed to steer the current velocity vector of the object outside the collision cone. This idea was later employed by many researchers for various applications ranging from aircraft conflict detection

and resolution [11], vision-based obstacle avoidance [12, 13], automobile collision avoidance [14], robotic collision avoidance [15], and to study collision avoidance behavior in biological organisms [16].

In subsequent work, collision cones have been extended to higher-dimensional spaces and general obstacle shapes [17]. They've also been used to design safe passage trajectories through narrow orifices for aerial as well as underwater vehicles [18]. In contrast to these prior research problems, the guidance laws presented in our work specify accelerations which when applied by a UAS enables it to steer its velocity vector *towards* the moving object and subsequently match its velocity to that of the object. The term rendezvous cone is more representative for this class of applications and we shall adopt this term in our presentation. In addition, our rendezvous cone approach employs vision-based information in order to perform its computations.

### B. Vision-Based Tracking

The first comprehensive survey on visual tracking and categorization of state-of-the-art algorithms was presented in [19]. Further research was provided by [20] and [21] where the main trends and taxonomy in object detection and tracking are introduced. Various vision-based tracking techniques exist ranging from low-level HSV threshold color-based detection [22, 23] through high-level tracking-by-detection learning-based methods [24, 25, 26]. To overcome known challenges in visual tracking, many ideas such as template matching [27], feature matching [28], and optical flow [29, 30, 31] have been adopted by researchers.

Our work focuses on visual object tracking [32, 33, 34, 35] utilizing a point estimator for target localization. In addition, we perform occlusion handling [36] and identify occlusion states [37, 38] along with case transitions for tracking point estimators. Tools and methods such as part-based templates [39], RGB color distributions [40], segmentation [41], deformable models [42], background/foreground [43] detection, etc., have been employed to carry out occlusion management. In comparison, our approach makes use of classical computer vision techniques [44]. Specifically, we implement a resilient feature detection strategy for tracking and adjusting the centroid of an object in the presence of extreme occlusions.

### III. PROBLEM STATEMENT

Consider a scenario in which a UAS, equipped with a downward-facing camera, is flying at a known altitude. In addition, the UAS only perceives visual information as it tracks a ground-based vehicle. It is assumed the vehicle has been detected and is initially within the UAS's field of view. Moreover, the motion of the vehicle is along a plane orthogonal to the principal axis of the camera and thus the image projection is orthographic. The problem is to develop vision-based guidance laws that facilitate the UAS in consistently tracking the vehicle even as it performs evasive maneuvers and encounters occlusions.

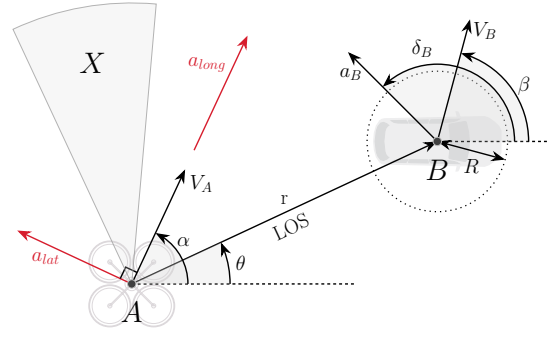


Fig. 2. An engagement between a UAS (A) and a ground vehicle (B).

### IV. VISION-BASED GUIDANCE

#### A. Engagement Geometry and Guidance Laws

We model the engagement geometry between a UAS (A) and vehicle (B) as an orthogonal projection onto a horizontal plane, Fig. 2. The UAS and vehicle are moving with speeds  $V_A$  and  $V_B$ , and heading angles  $\alpha$  and  $\beta$ , respectively. The distance between A and B is represented by  $r$  while  $\theta$  denotes the angle made by the line of sight (LOS) AB. The UAS has two control inputs: lateral acceleration  $a_{lat}$  and longitudinal acceleration  $a_{long}$ . Thus, A can rotate its velocity vector as well as change its speed. The vehicle can apply an acceleration of magnitude  $a_B$  which acts at an angle  $\delta_B$ , and  $R$  denotes the radius of B.  $X$  portrays the rendezvous cone from A to B. If A can steer its velocity vector into  $X$ , then A is on a trajectory that will cause it to rendezvous with B. The kinematics governing the engagement geometry are characterized by the equations governing AB,

$$\begin{bmatrix} \dot{r} \\ \dot{\theta} \\ \dot{V}_\theta \\ \dot{V}_r \\ \dot{\alpha} \\ \dot{V}_A \\ \dot{\beta} \\ \dot{V}_B \end{bmatrix} = \begin{bmatrix} V_r \\ V_\theta/r \\ -V_\theta V_r/r \\ V_\theta^2/r \\ 0 \\ 0 \\ 0 \\ 0 \end{bmatrix} + \begin{bmatrix} 0 \\ 0 \\ -\cos(\alpha - \theta) \\ \sin(\alpha - \theta) \\ 1/V_A \\ 0 \\ 0 \\ 0 \end{bmatrix} a_{lat} \quad (1)$$

$$+ \begin{bmatrix} 0 \\ 0 \\ -\sin(\alpha - \theta) \\ -\cos(\alpha - \theta) \\ 0 \\ 1 \\ 0 \\ 0 \end{bmatrix} a_{long} + \begin{bmatrix} 0 \\ 0 \\ \sin(\delta_B - \theta) \\ \cos(\delta_B - \theta) \\ 0 \\ 0 \\ \sin(\delta_B - \beta)/V_B \\ \cos(\delta_B - \beta) \end{bmatrix} a_B,$$

where  $V_r$  and  $V_\theta$  are the components of the relative velocity vector.

We define the rendezvous cone [10] as

$$y_1 = r^2 V_\theta^2 - R^2 (V_\theta^2 + V_r^2), \quad (2)$$

i.e., it is the cone of relative velocity vectors that will cause A to rendezvous with B. This is established by two conditions:

(i)  $y_1 < 0, V_r < 0$  and (ii)  $y_1 = 0, V_r < 0$ . Condition (i) corresponds to the case of the relative velocity vector being inside the rendezvous cone while condition (ii) corresponds to the scenario of the relative velocity vector being aligned with the boundary of the rendezvous cone. When (ii) occurs  $A$  will graze  $B$  at the instant of closest approach. We define the velocity matching error as

$$y_2 = V_r^2 + V_\theta^2. \quad (3)$$

Dynamic inversion is employed to drive the output functions to the desired values. By differentiating (2) and (3) we obtain the dynamic evolution of  $y_1$  and  $y_2$  as

$$\begin{bmatrix} \dot{y}_1 \\ \dot{y}_2 \end{bmatrix} = \begin{bmatrix} \frac{\partial y_1}{\partial r} & \frac{\partial y_1}{\partial \theta} & \frac{\partial y_1}{\partial V_\theta} & \frac{\partial y_1}{\partial V_r} \\ \frac{\partial y_2}{\partial r} & \frac{\partial y_2}{\partial \theta} & \frac{\partial y_2}{\partial V_\theta} & \frac{\partial y_2}{\partial V_r} \end{bmatrix} \times \begin{bmatrix} \dot{r} \\ \dot{\theta} \\ \dot{V}_\theta \\ \dot{V}_r \end{bmatrix}. \quad (4)$$

The partial derivatives of (4) are expressed as

$$\begin{bmatrix} 2rV_\theta^2 & 0 & 2V_\theta(r^2 - R^2) & -2r^2V_r \\ 0 & 0 & 2V_\theta & 2V_r \end{bmatrix}. \quad (5)$$

To calculate the required control input, we define two error quantities with respect to  $y_1$  and  $y_2$ . The error in  $y_1$  is specified as  $e_1(t) = y_{1d}(t) - y_1(t)$ , where  $y_{1d}(t) < 0$  is a reference input while the error in  $y_2$  is described as  $e_2(t) = 0 - y_2(t)$ . Taking  $y_{1d}(t)$  as a constant  $\forall t$ , we seek to determine  $a_{lat}$  and  $a_{long}$  which will ensure the error dynamics follow the equations  $\dot{e}_1 = -k_1 e_1$  and  $\dot{e}_2 = -k_2 e_2$  where  $k_1, k_2 > 0$  are constants. This in turn allows the quantities  $y_1$  and  $y_2$  to follow the dynamics, i.e.,

$$\begin{bmatrix} \dot{y}_1 \\ \dot{y}_2 \end{bmatrix} = \begin{bmatrix} k_1(y_{1d} - y_1) \\ -k_2 y_2 \end{bmatrix}. \quad (6)$$

After substituting (1), (5), and (6) into (4) we obtain

$$\begin{bmatrix} a_{11} & a_{12} \\ a_{21} & a_{22} \end{bmatrix} \begin{bmatrix} a_{lat} \\ a_{long} \end{bmatrix} = \begin{bmatrix} -k_1(y_{1d} - y_1)/2 \\ k_2 y_2/2 \end{bmatrix} - \begin{bmatrix} b_1 \\ b_2 \end{bmatrix} a_B, \quad (7)$$

where

$$\begin{aligned} a_{11} &= V_\theta(r^2 - R^2) \cos(\alpha - \theta) + R^2 V_r \sin(\alpha - \theta), \\ a_{12} &= V_\theta(r^2 - R^2) \sin(\alpha - \theta) + R^2 V_r \cos(\alpha - \theta), \\ a_{21} &= V_\theta \cos(\alpha - \theta) + V_r \sin(\alpha - \theta), \\ a_{22} &= V_\theta \sin(\alpha - \theta) + V_r \cos(\alpha - \theta), \\ b_1 &= V_r R^2 \cos(\delta_B - \theta) - V_\theta(r^2 - R^2) \sin(\delta_B - \theta), \\ b_2 &= -V_r \cos(\delta_B - \theta) - V_\theta \sin(\delta_B - \theta). \end{aligned}$$

By solving (7) we obtain

$$\begin{aligned} a_{lat} &= \left[ k_1(y_1 - y_{1d}) \left( V_r \cos(\alpha - \theta) + V_\theta \sin(\alpha - \theta) \right) \right. \\ &\quad + k_2 y_2 \left( V_r R^2 \cos(\alpha - \theta) - V_\theta(r^2 - R^2) \sin(\alpha - \theta) \right) \\ &\quad \left. - 2V_r V_\theta r^2 \sin(\alpha - \delta_B) a_B \right] / (2V_r V_\theta r^2) \end{aligned} \quad (8)$$

$$\begin{aligned} a_{long} &= \left[ k_1(y_1 - y_{1d}) \left( V_r \sin(\alpha - \theta) - V_\theta \cos(\alpha - \theta) \right) \right. \\ &\quad + k_2 y_2 \left( V_r R^2 \sin(\alpha - \theta) + V_\theta(r^2 - R^2) \cos(\alpha - \theta) \right) \\ &\quad \left. + 2V_r V_\theta r^2 \cos(\alpha - \delta_B) a_B \right] / (2V_r V_\theta r^2). \end{aligned} \quad (9)$$

(8) and (9) serve as the acceleration commands to the UAS and are supplied to our simulator. We note the acceleration commands  $a_{lat}(t)$  and  $a_{long}(t)$  depend on continuous feedback from the quantities  $y_1$  and  $y_2$ , states  $r, \theta, V_r, V_\theta$ , and the acceleration vector of the vehicle. The quantities  $r$  and  $\theta$  are obtained by direct measurements from the vision system while the remaining quantities are estimated using an acceleration model (Section IV-B).

### B. Vehicle Acceleration Model

The positional measurements of the vehicle in the image frame are obtained using feature point tracking (Section IV-E). In addition, since it's assumed the UAS knows its own states, we can transform the image measurements to an inertial frame. These inertial measurements are then fed into a linear acceleration model [45, 46]. The model filters the position data and provides estimates of the velocity and acceleration of the vehicle. Given that the position of the vehicle in the inertial frame is represented as  $(x_B, y_B)$ , we obtain the discrete form of the motion model as

$$\begin{aligned} \chi_B(k) &= \mathbf{F}_B \chi_B(k-1) + \mathbf{w}_B(k), \\ \mathbf{z}_B(k) &= \mathbf{H}_B \chi_B(k) + \mathbf{v}_B(k). \end{aligned} \quad (10)$$

where the state vector of the vehicle is represented by  $\chi_B = [x_B, \dot{x}_B, \ddot{x}_B, y_B, \dot{y}_B, \ddot{y}_B]^\top$  and  $\mathbf{z}_B$  is the measurement vector. The state transition matrix corresponding to the acceleration model is defined as

$$\mathbf{F}_B = \begin{bmatrix} \mathbf{T} & \mathbf{0} \\ \mathbf{0} & \mathbf{T} \end{bmatrix},$$

where  $\mathbf{0}$  is a  $3 \times 3$  matrix of zeros and

$$\mathbf{T} = \begin{bmatrix} 1 & \Delta t & [e^{-\alpha_B \Delta t} + \alpha_B \Delta t - 1]/\alpha_B^2 \\ 0 & 1 & [1 - e^{-\alpha_B \Delta t}]/\alpha_B \\ 0 & 0 & e^{-\alpha_B \Delta t} \end{bmatrix}.$$

The process noise is defined as  $\mathbf{w}_B \sim \mathcal{N}(0, \mathbf{Q}_B)$  and the noise covariance matrix is given by

$$\mathbf{Q}_B = 2\alpha_B \sigma_B^2 \begin{bmatrix} \mathbf{Q} & \mathbf{0} \\ \mathbf{0} & \mathbf{Q} \end{bmatrix},$$

where  $\alpha_B$ ,  $\sigma_B$ , and  $\mathbf{Q}$  are described in [45]. The size of  $\mathbf{Q}$  and  $\mathbf{0}$  is  $3 \times 3$ . The measurement matrix takes the form

$$\mathbf{H}_B = \begin{bmatrix} 1 & 0 & 0 & 0 & 0 & 0 \\ 0 & 0 & 0 & 1 & 0 & 0 \end{bmatrix}.$$

$\mathbf{v}_B \sim \mathcal{N}(0, \mathbf{R}_B)$  is the measurement noise and  $\mathbf{R}_B$  is the measurement noise covariance matrix. The velocity estimates  $(\dot{x}_B, \dot{y}_B)$  of the vehicle are transformed back into the UAS-centered relative frame to obtain the relative velocity components  $\hat{V}_r$  and  $\hat{V}_\theta$ . Similarly, the vehicle acceleration estimates  $(\ddot{x}_B, \ddot{y}_B)$  are translated into  $\hat{a}_B$  and  $\hat{\delta}_B$ .

### C. System Architecture

Our system architecture is shown in Fig 3. First, images captured by the UAS are used to estimate the relative and absolute position of the vehicle. Next, the measured velocity and acceleration states are processed to determine

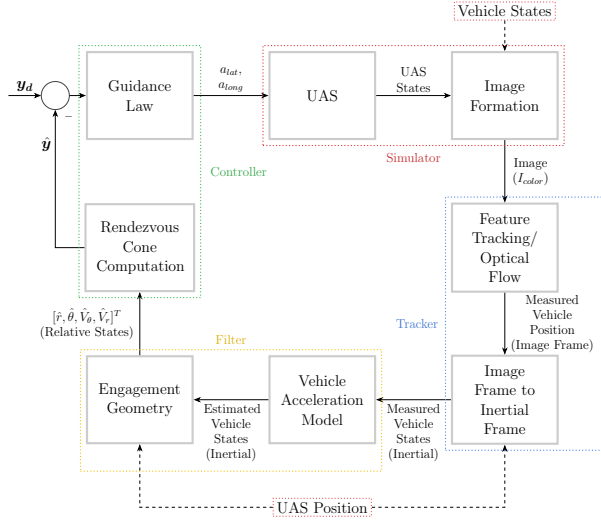


Fig. 3. The overall architecture of the vision-based guidance system.

the quantities  $[\hat{r}, \hat{\theta}, \hat{V}_\theta, \hat{V}_r, \hat{a}_B, \hat{\delta}_B]^\top$ . The filtered estimates of the noisy  $r_m$  and  $\theta_m$  measurements are represented by  $\hat{r}$  and  $\hat{\theta}$ ,  $\hat{V}_\theta$  and  $\hat{V}_r$  express approximations of the relative velocity components, and  $\hat{a}_B$  and  $\hat{\delta}_B$  represent estimates of the absolute acceleration magnitude and direction of the vehicle. Finally, these values are used to compute an assessment of the current rendezvous cone. An estimate of the UAS velocity vector with respect to the rendezvous cone is denoted by  $\hat{y}_1$ , while  $\hat{y}_2$  measures the magnitude of the relative velocity vector. The guidance algorithm generates suitable accelerations  $a_{lat}$  and  $a_{long}$  which drive  $\hat{y}_1$  and  $\hat{y}_2$  to the desired reference values. These accelerations move the UAS to a new position whereby an updated image of the scene is generated by the simulator.

#### D. Simulator

We have developed a Python Pygame [47] simulator that constructs orthographic projections from simulated kinematic states of a UAS and a vehicle. The simulator generates RGB images at the appropriate frame rates or time instances. Additionally, it can accept acceleration commands as input, update the kinematic states of the simulated entities governed by the laws of rigid body motion, and generate accurate renders. The simulator maps 3D scene points onto a 2D image plane of RGB triplets. More formally, we describe this as the composition of two mappings  $\mathcal{M}_1 : \mathbb{R}^3 \rightarrow \mathbb{P}^2$  and  $\mathcal{M}_2 : \mathbb{P}^2 \rightarrow \mathbb{R}^3$  which yields  $\mathcal{M}_2 \circ \mathcal{M}_1 : \mathbb{R}^3 \rightarrow \mathbb{R}^3$ . The mapping  $\mathcal{M}_1$  transforms kinematic states  ${}^W\mathbf{x}(t) = [{}^Wx(t), {}^Wy(t), {}^Wz(t)]^\top$  onto an orthographic projective space. It generates the homogeneous vector  $\tilde{\mathbf{x}}(t) = [\tilde{x}(t), \tilde{y}(t), \tilde{w}(t)]^\top = \tilde{w}[x(t), y(t), 1]^\top$  where  $\mathbf{x}(t) = [x(t), y(t)]^\top = \begin{bmatrix} \tilde{x}(t) \\ \tilde{y}(t) \\ \tilde{w}(t) \end{bmatrix}$ . Conversely, the mapping  $\mathcal{M}_2$  discretizes and maps  $\tilde{\mathbf{x}}(t)$  to image intensities  $I_{color}(x, y, t) = [r(t), g(t), b(t)]^\top$ . The colored image is converted to grayscale,  $I(x, y, t)$ , which is then consumed by the feature tracker. It's worth mentioning that the simulator renders are non-anti-aliased which introduces a discretization

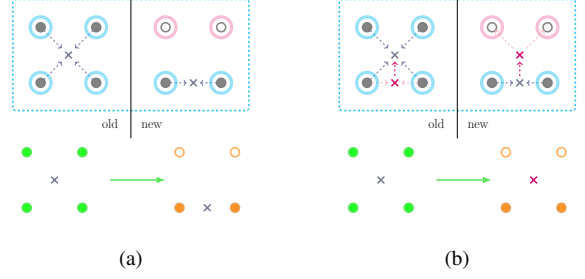


Fig. 4. Feature tracking for no occlusion to partial occlusion state transitions: (a) without centroid adjustment, (b) with centroid adjustment. ●—no occlusion, ●—partial occlusion, ●—good points (flow success), ●—bad points (flow failure), ●—visible points, ●—occluded points, ✕—not adjusted centroid, ✕—adjusted centroid, □—optical flow across old and new frames.

noise in the measurements since subpixel motions are not simulated.

#### E. Feature Tracker

1) *Optical Flow*: We obtain sparse optical flow at good and desirable feature points [48]. Feature points are good if the eigenvalues of the gradient matrix at that point are large and they are desirable if they correspond to the object to be tracked through a sequence of images. A Kanade-Lucas-Tomasi (KLT) tracker [49, 50] is used for the task of tracking feature point sets,  $\mathcal{F}^k = \{\mathbf{f}_i^k\}_{i=1}^n$ , where  $n$  is the number of points and  $\mathbf{f}_i^k = (x_i, y_i)^k$  is the  $i^{th}$  point in the  $k^{th}$  frame.

Optical flow displacements  $\mathbf{u}|_{\mathbf{f}_i \in \mathcal{F}}$ , where  $\mathbf{u} = [u_x, u_y, 1]^\top$ , are obtained under the assumption of a linearized brightness constancy [51],

$$I(x, y, t) = I(x + u_x, y + u_y, t + 1). \quad (11)$$

The displacements are computed over a small neighborhood  $\mathcal{N}_{\mathbf{f}_i}$  of each  $\mathbf{f}_i$ . This is done by solving a system of linear equations,

$$(\nabla I(\mathbf{x}))^\top \cdot \mathbf{u} = 0, \quad \forall \mathbf{x} \in \mathcal{N}_{\mathbf{f}}, \quad (12)$$

where  $\nabla = \left[ \frac{\partial}{\partial x}, \frac{\partial}{\partial y}, \frac{\partial}{\partial t} \right]^\top$  is the gradient operator. Using the computed displacement vectors, updated locations  $\mathbf{f}_i^{k+1} = (x_i, y_i)^{k+1}$  are obtained. Furthermore, a multiscale pyramidal [52, 53, 54] approach enables tracking of an object through larger displacements across frames.

2) *Centroid Adjustment*: Reliable optical flow computations require brightness constancy and temporal regularity at feature points across frames. What's more, spatial consistency such that pixels in the neighborhood of feature points have a motion similar to the point, is needed as well. In practice, flow computations can be brittle when factors such as nonlinear image distortions, noise, and occlusions occur. Moreover, we may experience  $m \leq n$  missing points caused by high flow optimization errors. This may result in unpredictable shifts in centroid location despite the tracked object being relatively stationary.

To mitigate these effects we implement centroid adjustment, i.e., the centroid of  $n$  feature points belonging to the



object is localized for consistent measurements. Formally, we define a centroid as

$$\bar{\mathcal{F}} = \frac{1}{n} \sum_{i=1}^n \mathbf{f}_i. \quad (13)$$

Adjustment of a centroid is then defined as

$$\Delta \bar{\mathcal{F}} = * \bar{\mathcal{F}}^{old} - {}^{good} \bar{\mathcal{F}}^{old}, \quad (14)$$

$$* \bar{\mathcal{F}}^{new} = {}^{good} \bar{\mathcal{F}}^{new} + \Delta \bar{\mathcal{F}}, \quad (15)$$

where  $\Delta \bar{\mathcal{F}}$  is the centroid adjustment and  $* \bar{\mathcal{F}}^{new}$  denotes the adjusted centroid. Pre-superscripts are used to indicate good, bad, or all (\*) points and post-superscripts mean an old or new frame. This process is depicted in Fig. 4.

Using centroid adjustment with the assumption of rigid shape constraints, if we compute good flow for at least one keypoint ( $m < n$ ), then we can obtain stable centroid measurements. Furthermore, for resilience purposes, feature and template matching are used as fallback techniques while handling occlusions. Even though the object of interest is primarily represented using Shi-Tomasi keypoints, we also have access to full and partial templates of the object. This includes SIFT [55] descriptors for redetection and recovery purposes.

#### F. Occlusion Handling

In presence of occlusions,  $|\mathcal{F}| = n$  cannot be assured. Besides,  $m > 0$  for at least  $n$  time instances guarantees measurements will vanish. In the context of tracking  $n$  feature points  $\{\mathbf{f}_i\}_{i=1}^n$ , we identify the following three occlusion states ( $\mathcal{O}$ ) with nine transitions among them: (i) no occlusion ( $\mathcal{N}$ ), (ii) partial occlusion ( $\mathcal{P}$ ), and (iii) total occlusion ( $\mathcal{T}$ ). The occlusion states can be detected and identified by drawing inference from the cardinality  $|\mathcal{F}|$ , i.e.,

$$\begin{aligned} |\mathcal{F}| = n &\implies \mathcal{N} \\ 0 < |\mathcal{F}| \leq n &\implies \mathcal{P} \\ |\mathcal{F}| = 0 &\implies \mathcal{T}. \end{aligned} \quad (16)$$

Although detecting states of occlusion is elementary, treating different occlusion states in order to perform long-term point tracking via optical flow is challenging. This is due to the fact that optical flow depends on the health of the keypoints not only in the current frame, but also from the previous frame. Consequently, to handle occlusions we enumerate nine transition instances as shown in Fig. 5c. Observe in Fig. 5b that the *no occlusion* state set  $\mathcal{N}$  and the *total occlusion* state set  $\mathcal{T}$  are singletons. Yet, the *partial occlusion* state is a finite set  $\mathcal{P} = \{\mathcal{F} \mid 0 < |\mathcal{F}| \leq n\}$  with multiple elements. Accordingly, cases 1, 3, 7, 9 are the easiest to handle, cases 2, 4, 6, 8 are moderate in complexity, and case 5 is the most complex. A further breakdown of case 5 is discussed in Section IV-F.2.

1) *From No Occlusion* ( $\mathcal{O}^{old} = \mathcal{N}$ ): In this situation we have  $|\mathcal{F}^{old}| = n$  and optical flow can be computed for feature points  ${}^{good} \mathcal{F}^{old}$  to obtain  ${}^{good} \mathcal{F}^{new}$ . The occlusion state identification in the new frame ( $\mathcal{O}^{new}$ ) can be carried out reliably as per (16). Furthermore, by using the adjusted centroid, missing keypoints  ${}^{bad} \mathcal{F}^{new}$  can be back projected and reconstructed as displayed in Fig. 6. Occlusions cause these points to be lost (Fig. 6a), however (for cases 1, 2, 3, 5, 6) with reconstruction the missing points can be fully recovered (Fig. 6b).

2) *From Partial Occlusion* ( $\mathcal{O}^{old} = \mathcal{P}$ ): Here we have  $0 < |\mathcal{F}^{old}| \leq n$  and optical flow can be calculated at feature points  ${}^{good} \mathcal{F}^{old}$ . However, the identification of occlusion state ( $\mathcal{O}^{new}$ ) is not trivial and (16) cannot be reliably used. Therefore, we identify the following six subcases (Fig. 7): (a)  ${}^{good} \mathcal{F}^{new} = {}^{good} \mathcal{F}^{old}$ , (b)  ${}^{good} \mathcal{F}^{new} \supset {}^{good} \mathcal{F}^{old}$ , (c)  ${}^{good} \mathcal{F}^{new} \subset {}^{good} \mathcal{F}^{old}$ , (d)  ${}^{good} \mathcal{F}^{new} \cap {}^{good} \mathcal{F}^{old} = \emptyset$ , (e)  ${}^{good} \mathcal{F}^{new} \subset {}^{bad} \mathcal{F}^{old}$ , and (f)  ${}^{good} \mathcal{F}^{new} \cap {}^{good} \mathcal{F}^{old} \neq \emptyset$  (exclusive of other subcases). Optical flow can be successfully determined in subcases 5a, 5b, 5c, 5f, or case 4, while subcases 5d, 5e, or case 6 indicates failure. To perform robust tracking with occlusions we need to accurately identify the occlusion states. In the partial-partial case, SIFT feature matching or part-based template matching can be used. The subcase treatments can be summarized as follows: 5a requires no further processing, 5b necessitates redetection of the points, 5c involves missing point reconstruction, 5f needs both redetection and missing point reconstruction, 5d and 5e call for redetection using matching techniques.

3) *From Total Occlusion* ( $\mathcal{O}^{old} = \mathcal{T}$ ): In this circumstance we have  $|\mathcal{F}^{old}| = 0$ , hence optical flow computations cannot be made. To continue tracking for cases 7, 8, 9 we can use techniques, such template or feature matching, and redetect initial/updated feature points  ${}^{good} \mathcal{F}^0$  in the new frame to obtain  ${}^{good} \mathcal{F}^{new}$ . Occlusion state identification ( $\mathcal{O}^{new}$ ) can then be decisively carried out as per (16).

#### G. Image Formation

Using optical flow, centroid adjustment, and occlusion handling mechanisms, we can obtain noisy but accurate localization measurements of the vehicle  $\mathbf{x}_B$  from the image plane to the world inertial frame as follows. The altitude  ${}^W z_A(t)$  and camera calibration information such as field of view ( $\vartheta = 47^\circ$ ) and image sensor width ( $\mathcal{W} = 5 \text{ mm}$ ) are all known. Therefore, with a pixel size of  $6.25 \mu\text{m}$  we can calculate the camera focal length as

$$\varphi = \frac{\mathcal{W}}{2} \left[ \tan \left( \frac{\vartheta}{2} \right) \right]^{-1}. \quad (17)$$

Under orthographic projection of objects moving on a plane, (17) can be used to obtain a mapping from image coordinates  $\mathbf{x}_B$  to world coordinates  ${}^W \mathbf{x}_B$  by the geometric relation

$${}^W \mathbf{x}_B = \frac{{}^W z_A(t)}{\varphi} \mathbf{x}_B. \quad (18)$$

Thus, (18) allows us to compute the measured kinematics state vector  $[{}^W \mathbf{x}_B^\top, {}^W \dot{\mathbf{x}}_B^\top]^\top$  of the vehicle in planar world

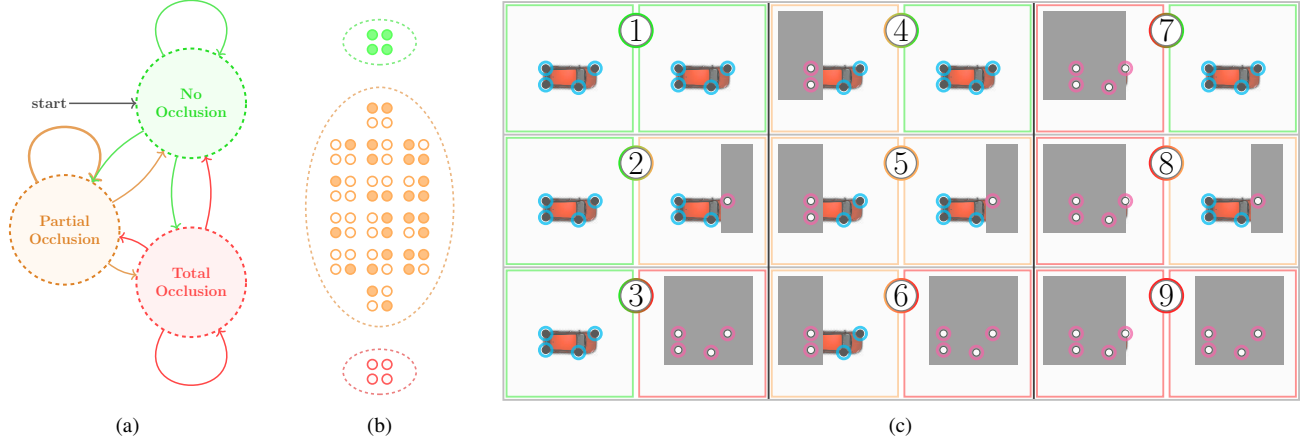


Fig. 5. (a) Occlusion state transitions. (b) Occlusion state sets: **No Occlusion** (top), **Partial Occlusion** (middle), **Total Occlusion** (bottom). (c) Enumerated occlusion state transition case instances are depicted with a vehicle and occlusion bars as follows: cases (1-3) enumerate transitions from *no occlusion* to *no*, *partial*, *total occlusion*; cases (4-6) enumerate transitions from *partial occlusion* to *no*, *partial*, *total occlusion*; and cases (7-9) enumerate transitions from *total occlusion* to *no*, *partial*, *total occlusion*. ●-good points (flow success), ●-bad points (flow failure), ●-visible points, ●-occluded points.

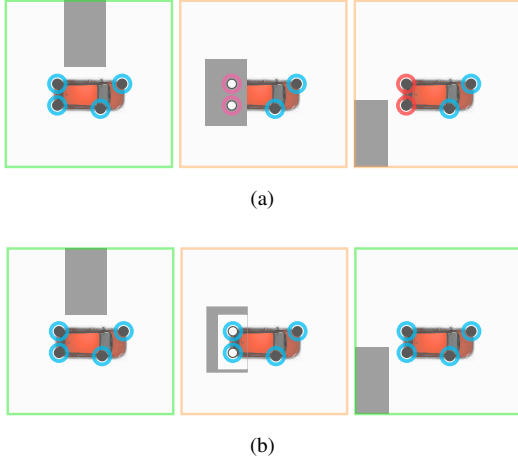


Fig. 6. Three consecutive frames with partial occlusions in the middle frame. (a) Keypoints lost without missing point reconstruction, and (b) keypoints recovered with missing point reconstruction. ●-good points (flow success/recovered), ●-bad points (flow failure), ●-lost points, ●-visible points, ●-occluded points.

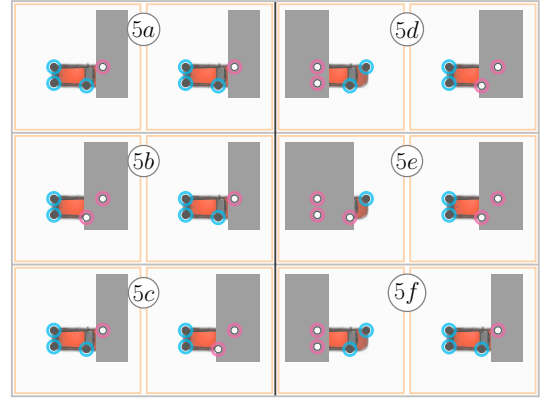


Fig. 7. Partial-partial occlusion state transition subcase instances. Subcases (5a-5f) represent equal, proper superset, proper subset, equal to complement, proper subset of complement, and non-empty intersection, respectively. ●-good points (flow success), ●-bad points (flow failure), ●-visible points, ●-occluded points.

coordinates. Finally,  $[{}^W x_B, {}^W y_B]^\top$  is converted to polar form  $(r, \theta)$ .

## V. SIMULATIONS

In this section, we demonstrate the behavior of our vision-based guidance framework using the following (unknown to the UAS) vehicle trajectory variants: lane changing and squircle following. All simulations were performed on a Windows 10 machine with an Intel Core i7-8700 CPU and 32 GB RAM. For every simulation, we make use of the true values of each quantity alongside their measured and/or estimated values to generate the data plots.

1) *Lane Changing Trajectory*: We simulate the vehicle to move in the east direction while performing lane changing maneuvers of approximately 4 m at arbitrary time instances with occlusions. The UAS starts at position  ${}^W x_{A0} =$

$[0.0, 0.0, 150.0]^\top (m)$  while the vehicle begins at  ${}^W x_{B0} = [50.0, -30.0, 0.0]^\top (m)$  with speeds  ${}^W V_{A0} = 31.31 (m/s)$  (70 mph) and  ${}^W V_{B0} = 22.22 (m/s)$  (50 mph), and headings  ${}^W \alpha_0 = 0.0^\circ$  and  ${}^W \beta_0 = 0.0^\circ$ , respectively. The simulation was run for approximately 149 secs. Fig. 8 depicts the kinematic state information collected over time. Under total occlusions, measurements disappear and state estimations are utilized to perform guidance. It can be observed in the data plots that estimations may veer away from the true values if an occlusion persists for a long time. In the simulations, the occurrence of occlusions is accompanied by an increasing covariance ( $\mathbf{R}_B$ ) in the measurement noise ( $\mathbf{v}_B$ ) in (10) and by employing previous estimates as current measurements in the acceleration model. In Fig. 9, the speed and heading profiles of the UAS and vehicle along with their deltas are provided. The trajectories of the UAS and vehicle in world and camera reference frames are shown in Fig. 10. Visual

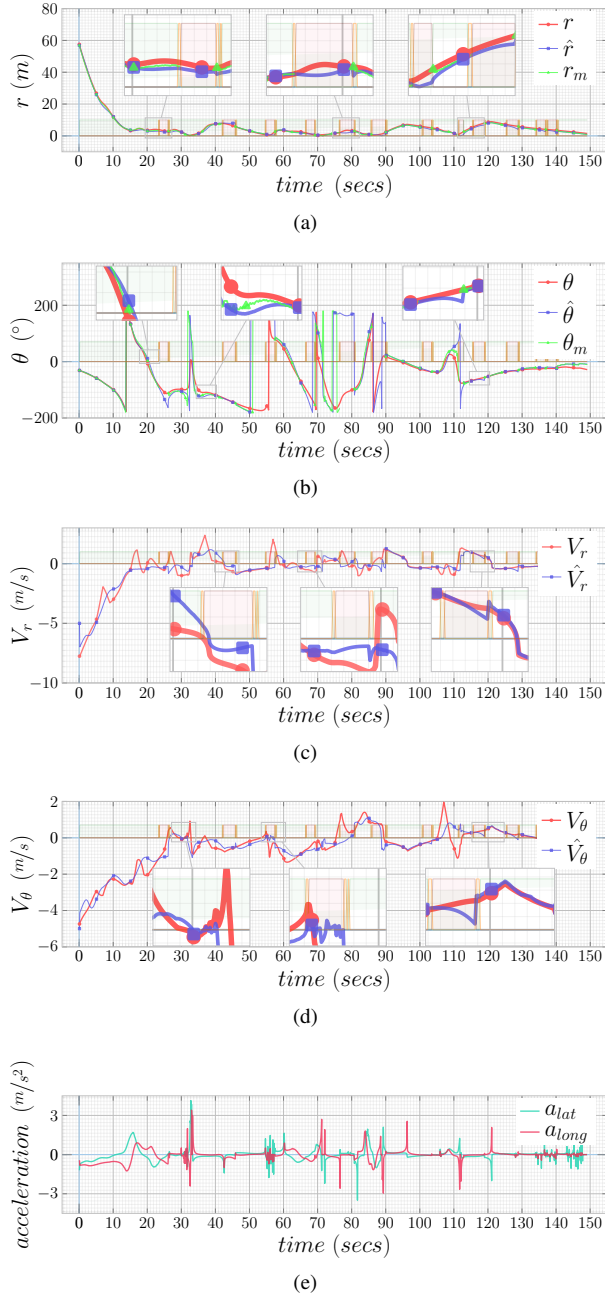


Fig. 8. Lane changing trajectory: (a)-(d) true, estimated, and measured states  $r$ ,  $\theta$ ,  $V_r$ , and  $V_\theta$ ; (e) acceleration commands  $a_{lat}$  and  $a_{long}$ . No (pink), partial (orange), and total (green) occlusion states are indicated along the zero line.

tracking was successfully performed using our occlusion handling and rendezvous cone-based guidance scheme.

2) *Squirrel Following Trajectory*: We simulate the vehicle to proceed along a parameterized squircular trajectory such that it traverses the closed curve with a period of 360 secs. The UAS begins at position  ${}^W\mathbf{x}_{A0} = [0.0, 0.0, 350.0]^\top (m)$  with speed  ${}^WV_{A0} = 31.31 (m/s)$  (70 mph) while the vehicle starts at  ${}^W\mathbf{x}_{B0} = [0.0, -20.0, 0.0]^\top (m)$ . Both the UAS and vehicle have an initial heading of  ${}^W\alpha_0 = 0.0^\circ$  and  ${}^W\beta_0 = 0.0^\circ$ . The vehicle speed  ${}^WV_B$  decreases around the corners to approximately 14.79 (m/s) (33.08 mph) while it

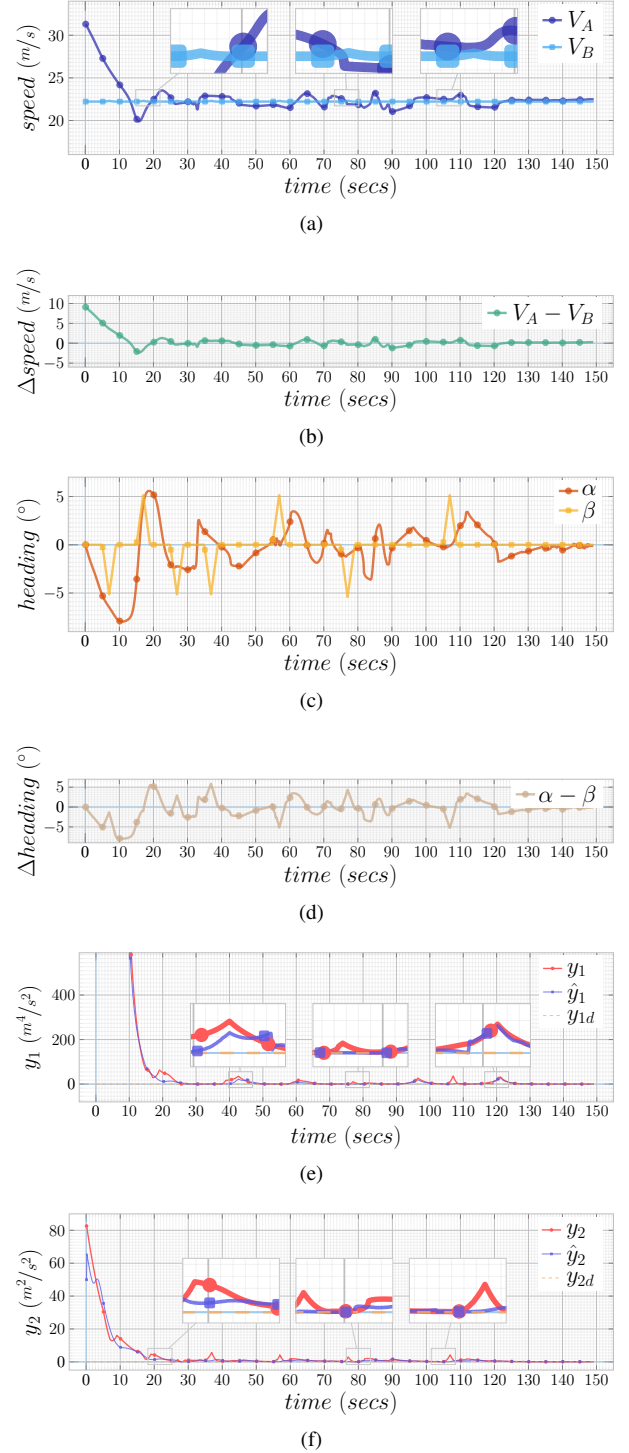


Fig. 9. Lane changing trajectory: (a) speed of the UAS and vehicle and (b) their differences; (c) heading of the UAS and vehicle and (b) their differences; (e)-(f) true and estimated objective functions  $y_1$  and  $y_2$ .

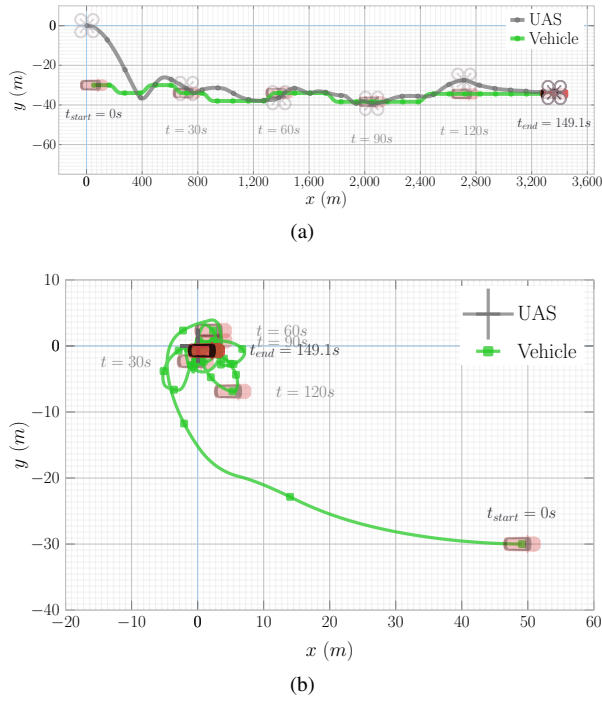


Fig. 10. Lane changing trajectory: UAS and vehicle trajectories in world (a) and camera (b) reference frames.

reaches nearly  $22.63 \text{ (m/s)}$  ( $50.62 \text{ mph}$ ) along the straight ways. The simulation was run for about  $671 \text{ secs}$ . In Fig. 11, the true, estimated, and measured kinematics states along with the lateral and longitudinal accelerations are shown. The speed, heading, and deltas are visualized in Fig. 12 along with the true and estimated objective functions  $y_1$  and  $y_2$ . Fig. 13 depicts the trajectories of the UAS and vehicle in world and camera frames of reference. Our vision-based guidance system was able to successfully allow the UAS to chase the vehicle while matching its speed and heading at non-constant velocities.

## VI. CONCLUSION AND FUTURE WORK

In conclusion, we have presented our solution to a problem wherein a UAS must track a ground-based vehicle moving at erratic velocities through occlusions using only visual information from a single camera. A rendezvous cone guidance scheme drives our objective functions to the desired values resulting in the generation of acceleration commands that lead the UAS into the cone and towards the vehicle. We perform visual tracking of the vehicle's centroid using feature detection and optical flow along with a diagnosis and analysis of occlusion events. A publicly available simulator that provides an environment to perform these vision-based guidance simulations has been developed. In the future, we plan to extend the guidance strategy to 3D, incorporate multi-vehicle tracking, and improve the fidelity of the simulator.

## ACKNOWLEDGMENTS

This material is based in part upon work supported by the National Science Foundation through grant #IIS-1851817

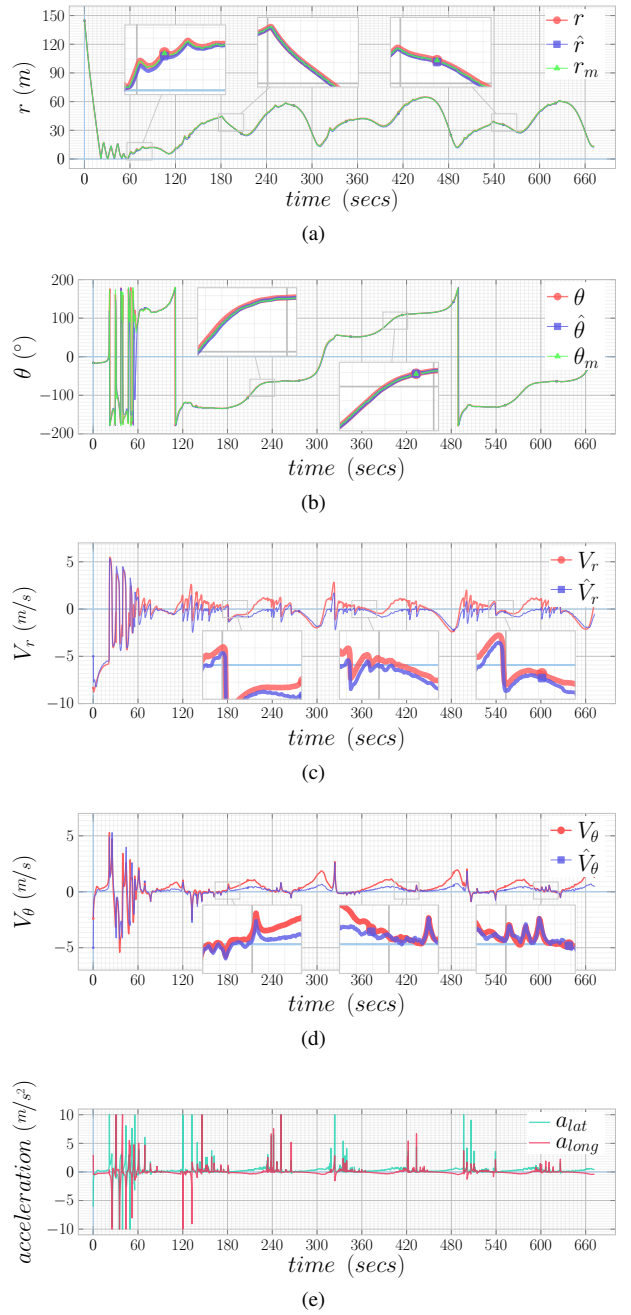


Fig. 11. Squirrel following trajectory: (a)-(d) true, estimated, and measured states  $r$ ,  $\theta$ ,  $V_r$ , and  $V_\theta$ ; (e) acceleration commands  $a_{lat}$  and  $a_{long}$ .

and a University of Texas at Arlington Research Enhancement Program grant #270079.

## REFERENCES

- [1] C. Kanellakis and G. Nikolakopoulos, "Survey on computer vision for uavs: Current developments and trends," *Journal of Intelligent & Robotic Systems*, vol. 87, no. 1, pp. 141–168, 2017.
- [2] A. Al-Kaff, D. Martin, F. Garcia, A. de la Escalera, and J. M. Armingol, "Survey of computer vision algorithms and applications for unmanned aerial vehicles," *Expert Systems with Applications*, vol. 92, pp. 447–463, 2018.
- [3] K. Kanistras, G. Martins, M. J. Rutherford, and K. P. Valavanis, "A survey of unmanned aerial vehicles (uavs) for traffic monitoring," in *Proceedings of the International Conference on Unmanned Aircraft Systems (ICUAS)*, 2013, pp. 221–234.



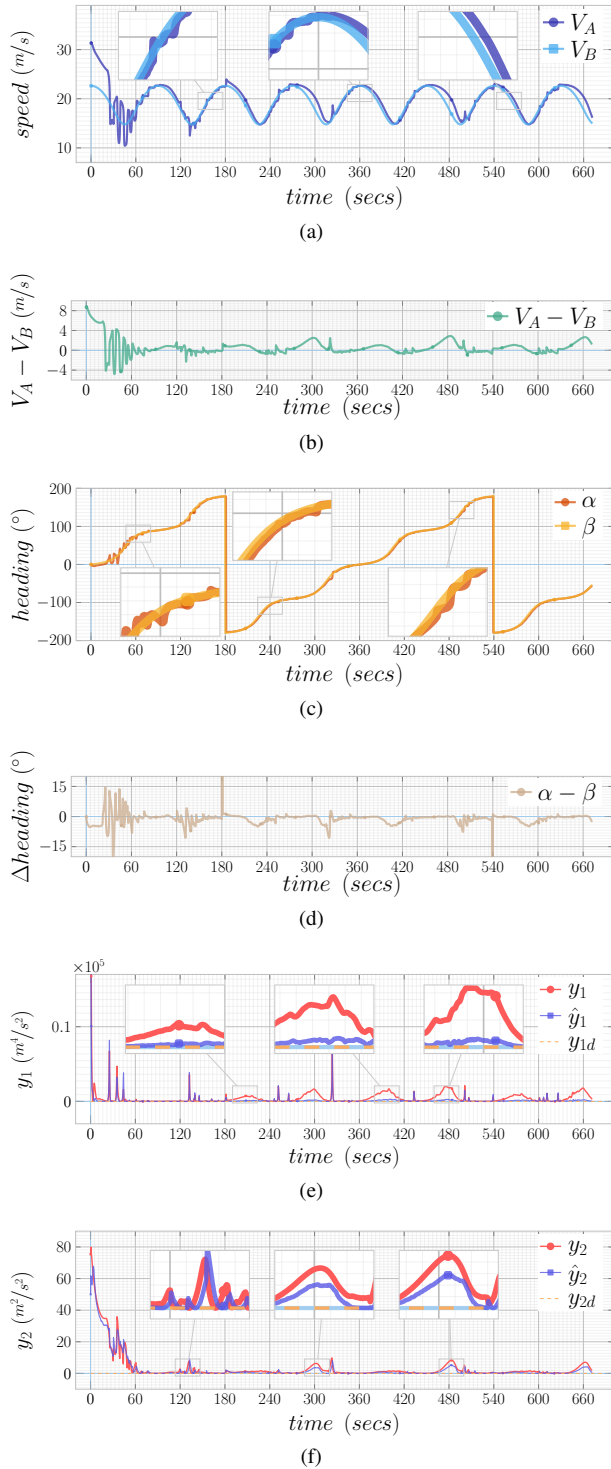


Fig. 12. Squirrel following trajectory: (a) speed of the UAS and vehicle and (b) their differences; (c) heading of the UAS and vehicle and (d) their differences; (e)-(f) true and estimated objective functions  $y_1$  and  $y_2$ .

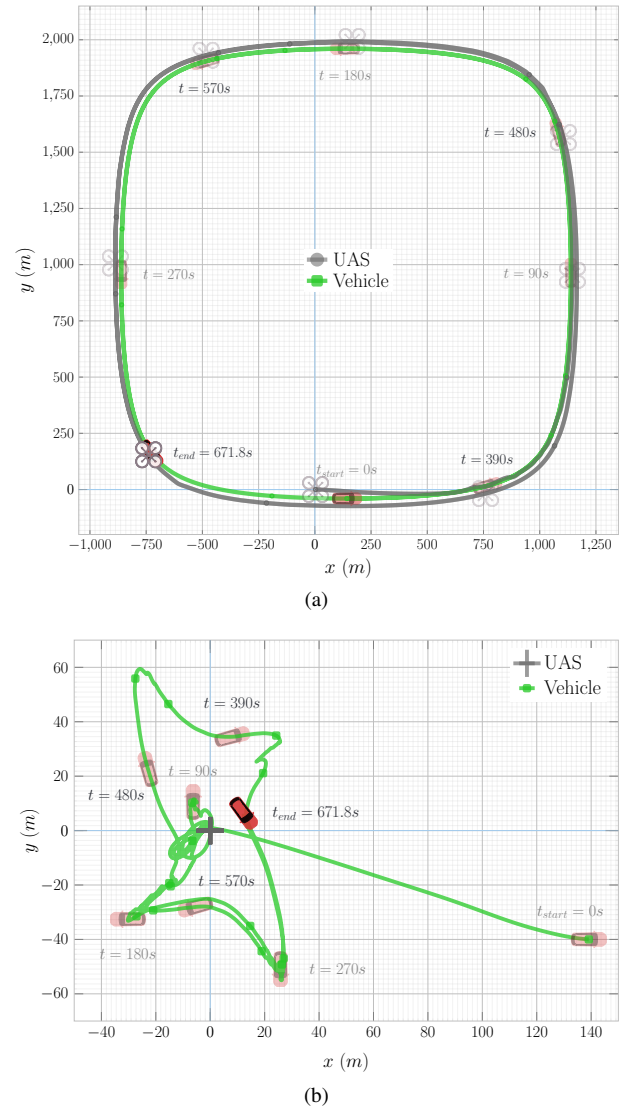


Fig. 13. Squirrel following trajectory: UAS and vehicle trajectories in world (a) and camera (b) frames of reference.

- [4] H. Zhou, H. Kong, L. Wei, D. Creighton, and S. Nahavandi, "Efficient road detection and tracking for unmanned aerial vehicle," *IEEE Transactions on Intelligent Transportation Systems*, vol. 16, no. 1, pp. 297–309, 2014.
- [5] S. Yeong, L. King, and S. Dol, "A review on marine search and rescue operations using unmanned aerial vehicles," *International Journal of Marine and Environmental Sciences*, vol. 9, no. 2, pp. 396–399, 2015.
- [6] C. Van Tilburg, "First report of using portable unmanned aircraft systems (drones) for search and rescue," *Wilderness & Environmental Medicine*, vol. 28, no. 2, pp. 116–118, 2017.
- [7] T. Samad, J. S. Bay, and D. Godbole, "Network-centric systems for military operations in urban terrain: The role of uavs," *Proceedings of the IEEE*, vol. 95, no. 1, pp. 92–107, 2007.
- [8] S. G. Manyam, S. Rasmussen, D. W. Casbeer, K. Kalyanam, and S. Manickam, "Multi-uav routing for persistent intelligence surveillance & reconnaissance missions," in *Proceedings of the International Conference on Unmanned Aircraft Systems (ICUAS)*. IEEE, 2017, pp. 573–580.
- [9] <https://github.com/robotic-vision-lab/Vision-Based-Object-Tracking>.
- [10] A. Chakravarthy and D. Ghose, "Obstacle avoidance in a dynamic environment: A collision cone approach," *IEEE Transactions on Systems, Man, and Cybernetics-Part A: Systems and Humans*, vol. 28, no. 5, pp. 562–574, 1998.
- [11] J. Goss, R. Rajvanshi, and K. Subbarao, "Aircraft conflict detection

- and resolution using mixed geometric and collision cone approaches,” in *AIAA Guidance, Navigation, and Control Conference and Exhibit*, 2004, p. 4879.
- [12] Y. Watanabe, A. Calise, E. Johnson, and J. Evers, “Minimum-effort guidance for vision-based collision avoidance,” in *AIAA Atmospheric Flight Mechanics Conference and Exhibit*, 2006, p. 6641.
  - [13] Y. Watanabe, A. Calise, and E. Johnson, “Vision-based obstacle avoidance for uavs,” in *AIAA Guidance, Navigation and Control Conference and Exhibit*, 2007, p. 6829.
  - [14] A. Ferrara and C. Vecchio, “Second order sliding mode control of vehicles with distributed collision avoidance capabilities,” *Mechatronics*, vol. 19, no. 4, pp. 471–477, 2009.
  - [15] B. Gopalakrishnan, A. K. Singh, and K. M. Krishna, “Time scaled collision cone based trajectory optimization approach for reactive planning in dynamic environments,” in *Proceedings of the IEEE/RSJ International Conference on Intelligent Robots and Systems (IROS)*, 2014, pp. 4169–4176.
  - [16] N. L. Brace, T. L. Hedrick, D. H. Theriault, N. W. Fuller, Z. Wu, M. Betke, J. K. Parrish, D. Grünbaum, and K. A. Morgansen, “Using collision cones to assess biological deconfliction methods,” *Journal of the Royal Society Interface*, vol. 13, no. 122, p. 20160502, 2016.
  - [17] A. Chakravarthy and D. Ghose, “Collision cones for quadric surfaces in  $n$ -dimensions,” *IEEE Robotics and Automation Letters*, vol. 3, no. 1, pp. 604–611, 2017.
  - [18] W. Zuo, K. Dhal, A. Keow, A. Chakravarthy, and Z. Chen, “Model-based control of a robotic fish to enable 3d maneuvering through a moving orifice,” *IEEE Robotics and Automation Letters*, vol. 5, no. 3, pp. 4719–4726, 2020.
  - [19] A. Yilmaz, “Object tracking and activity recognition in video acquired using mobile cameras,” Ph.D. dissertation, University of Central Florida, 2004.
  - [20] A. Yilmaz, O. Javed, and M. Shah, “Object tracking: A survey,” *ACM Computing Surveys (CSUR)*, vol. 38, no. 4, pp. 13–es, 2006.
  - [21] F. Porikli and A. Yilmaz, “Object detection and tracking,” in *Video Analytics for Business Intelligence*. Springer, 2012, pp. 3–41.
  - [22] R. Carelli, C. M. Soria, and B. Morales, “Vision-based tracking control for mobile robots,” in *Proceedings of the International Conference on Advanced Robotics (ICAR)*. IEEE, 2005, pp. 148–152.
  - [23] H. Lee, S. Jung, and D. H. Shim, “Vision-based uav landing on the moving vehicle,” in *Proceedings of the International Conference on Unmanned Aircraft Systems (ICUAS)*. IEEE, 2016, pp. 1–7.
  - [24] J. F. Henriques, R. Caseiro, P. Martins, and J. Batista, “High-speed tracking with kernelized correlation filters,” *IEEE Transactions on Pattern Analysis and Machine Intelligence (PAMI)*, vol. 37, no. 3, pp. 583–596, 2014.
  - [25] P. Bergmann, T. Meinhardt, and L. Leal-Taixe, “Tracking without bells and whistles,” in *Proceedings of the International Conference on Computer Vision (ICCV)*. IEEE, 2019, pp. 941–951.
  - [26] X. Zhou, V. Koltun, and P. Krähenbühl, “Tracking objects as points,” in *Proceedings of the European Conference on Computer Vision (ECCV)*. Springer, 2020, pp. 474–490.
  - [27] J. Pan and B. Hu, “Robust occlusion handling in object tracking,” in *Proceedings of the IEEE Conference on Computer Vision and Pattern Recognition (CVPR)*. IEEE, 2007, pp. 1–8.
  - [28] S. Shen, Y. Mulgaonkar, N. Michael, and V. Kumar, “Vision-based state estimation and trajectory control towards high-speed flight with a quadrotor,” in *Robotics: Science and Systems*, vol. 1. Citeseer, 2013, p. 32.
  - [29] V. K. Madasu and M. Hanmandlu, “Estimation of vehicle speed by motion tracking on image sequences,” in *IEEE Intelligent Vehicles Symposium*, 2010, pp. 185–190.
  - [30] B. Li, W. Wu, Q. Wang, F. Zhang, J. Xing, and J. Yan, “Siamrpn++: Evolution of siamese visual tracking with very deep networks,” in *Proceedings of the IEEE Conference on Computer Vision and Pattern Recognition (CVPR)*, 2019, pp. 4282–4291.
  - [31] Q. Wang, L. Zhang, L. Bertinetto, W. Hu, and P. H. Torr, “Fast online object tracking and segmentation: A unifying approach,” in *Proceedings of IEEE Conference on Computer Vision and Pattern Recognition (CVPR)*, 2019, pp. 1328–1338.
  - [32] V. N. Dobrokhodov, I. I. Kaminer, K. D. Jones, and R. Ghabcheloo, “Vision-based tracking and motion estimation for moving targets using small uavs,” in *Proceedings of the American Control Conference (ACC)*. IEEE, 2006, pp. 6–pp.
  - [33] B. Jeon, K. Baek, C. Kim, and H. Bang, “Mode changing tracker for ground target tracking on aerial images from unmanned aerial vehicles,” in *Proceedings of the (ICCAS)*. IEEE, 2013, pp. 1849–1853.
  - [34] Y. Kim, W. Jung, and H. Bang, “Visual target tracking and relative navigation for unmanned aerial vehicles in a gps-denied environment,” *International Journal of Aeronautical and Space Sciences*, vol. 15, no. 3, pp. 258–266, 2014.
  - [35] S. Liu, S. Wang, W. Shi, H. Liu, Z. Li, and T. Mao, “Vehicle tracking by detection in uav aerial video,” *Science China Information Sciences*, vol. 62, no. 2, p. 24101, 2019.
  - [36] B. Y. Lee, L. H. Liew, W. S. Cheah, and Y. C. Wang, “Occlusion handling in videos object tracking: A survey,” in *IOP Conference Series: Earth and Environmental Science*, vol. 18, no. 1. IOP Publishing, 2014, p. 012020.
  - [37] A. Galton, “Lines of sight,” in *AISB Workshop on Spatial and Spatio-Temporal Reasoning*, vol. 35, 1994, pp. 37–39.
  - [38] C. Köhler, “The occlusion calculus,” in *Cognitive Vision Workshop*. Citeseer, 2002, pp. 420–450.
  - [39] T. Zhang, K. Jia, C. Xu, Y. Ma, and N. Ahuja, “Partial occlusion handling for visual tracking via robust part matching,” in *Proceedings of the IEEE Conference on Computer Vision and Pattern Recognition (CVPR)*, 2014, pp. 1258–1265.
  - [40] W. Bouachir and G.-A. Bilodeau, “Structure-aware keypoint tracking for partial occlusion handling,” in *Winter Conference on Applications of Computer Vision (WACV)*. IEEE, 2014, pp. 877–884.
  - [41] B. Han, C. Paulson, T. Lu, D. Wu, and J. Li, “Tracking of multiple objects under partial occlusion,” in *Automatic Target Recognition XIX*, vol. 7335. International Society for Optics and Photonics, 2009, p. 733515.
  - [42] C. C. C. Pang, W. W. L. Lam, and N. H. C. Yung, “A novel method for resolving vehicle occlusion in a monocular traffic-image sequence,” *IEEE Transactions on Intelligent Transportation Systems*, vol. 5, no. 3, pp. 129–141, 2004.
  - [43] P. Guha, A. Mukerjee, and V. K. Subramanian, “Formulation, detection and application of occlusion states (oc-7) in the context of multiple object tracking,” in *Proceedings of the International Conference on Advanced Video and Signal Based Surveillance (AVSS)*. IEEE, 2011, pp. 191–196.
  - [44] B. Zhou, P. Krähenbühl, and V. Koltun, “Does computer vision matter for action?” *arXiv preprint arXiv:1905.12887*, 2019.
  - [45] R. A. Singer, “Estimating optimal tracking filter performance for manned maneuvering targets,” *IEEE Transactions on Aerospace and Electronic Systems*, no. 4, pp. 473–483, 1970.
  - [46] P. R. Mahapatra and K. Mehrotra, “Mixed coordinate tracking of generalized maneuvering targets using acceleration and jerk models,” *IEEE Transactions on Aerospace and Electronic Systems*, vol. 36, no. 3, pp. 992–1000, 2000.
  - [47] Open-Source Community, *Pygame 2*, 2021, <https://www.pygame.org>.
  - [48] J. Shi and C. Tomasi, “Good features to track,” in *Proceedings of IEEE Conference on Computer Vision and Pattern Recognition (CVPR)*, 1994, pp. 593–600.
  - [49] B. D. Lucas and T. Kanade, “An iterative image registration technique with an application to stereo vision,” in *Proceedings of the International Joint Conference on Artificial Intelligence (IJCAI)*. Vancouver, British Columbia, 1981.
  - [50] C. Tomasi and T. Kanade, “Detection and tracking of point features,” CMU-CS-91-132, Carnegie Mellon University, Tech. Rep., 1991.
  - [51] B. K. Horn and B. G. Schunck, “Determining optical flow,” in *Techniques and Applications of Image Understanding*, vol. 281. International Society for Optics and Photonics, 1981, pp. 319–331.
  - [52] E. Memin and P. Perez, “A multigrid approach for hierarchical motion estimation,” in *Proceedings of the International Conference on Computer Vision (ICCV)*. IEEE, 1998, pp. 933–938.
  - [53] T. Brox, A. Bruhn, N. Papenberg, and J. Weickert, “High accuracy optical flow estimation based on a theory for warping,” in *Proceedings of the European Conference on Computer Vision (ECCV)*. Springer, 2004, pp. 25–36.
  - [54] A. Bruhn and J. Weickert, “Towards ultimate motion estimation: Combining highest accuracy with real-time performance,” in *Proceedings of the International Conference on Computer Vision (ICCV)*, vol. 1. IEEE, 2005, pp. 749–755.
  - [55] D. G. Lowe, “Distinctive image features from scale-invariant keypoints,” *International Journal of Computer Vision*, vol. 60, no. 2, pp. 91–110, 2004.